BOLETIN DE LA SOCIEDAD ESPAÑOLA DE
Cerámica y Vidrio
www.elsevier.es/bsecv

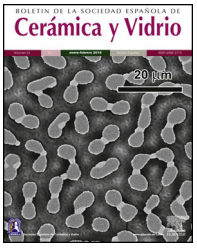

Original

Effects of Fe_2O_3 substitution for K_2O on the physical properties of $88P_2O_5$–xFe_2O_3–2CoO–$(10-x)K_2O$ glasses

Noureddine Bjaoui[a,b], *Nasr Sdiri*[a,*], *Manuel Almaida Valente*[c], *Karima Horchani-Naifer*[a], *Mokhtar Férid*[a]

[a] *Laboratoire de physico-chimie des matériaux minéraux et leurs applications, Centre National de Recherches en Sciences des Matériaux, B.P. 95 Hammam-Lif 2050, Tunisia*
[b] *Faculté des Sciences de Bizerte, Jarzouna 7021, Tunisia*
[c] *Department of Physics, I3N, University of Aveiro, 3810-193 Aveiro, Portugal*

ARTICLE INFO

Article history:
Received 28 October 2019
Accepted 6 February 2020
Available online 6 March 2020

Keywords:
Glasses
Calorimetry
Hysteresis
Gap energy
Impedance spectroscopy
Modulus

ABSTRACT

$88P_2O_5$–xFe_2O_3–2CoO–$(10-x)K_2O$ glasses from $x = 0.0$ to $x = 0.5$ were prepared at 850 °C using melt quenching technique.

These glass systems were characterized by using X-ray diffraction, differential scanning calorimetry (DSC), magnetic measurements, Raman spectroscopy, Archimedes methods, Brewster spectrometer, UV–vis spectrophotometer and impedance spectroscopy. X-ray diffraction revealed that these glass systems have amorphous structure. DSC has showed that the thermal stability of the glass samples increased with the rate of iron. Raman spectra showed the presence of the P–O–Fe group which increases the rigidity of the glass samples. The density of our compounds increased with the increase of the amount of iron oxide.

Magnetic measurements at 5 K using vibrating sample magnetometer technique show antiferromagnetic behavior of these system glasses.

According to the results of the optical absorption spectra, the values of the gap energy and Urbach energy decreased and the refractive index of the glass increased with the increase of the mole of Fe_2O_3. Brewster spectrophotometer has showed an optical index ($n > 1.5$). On other hand, the chromatic coordinates of all samples to the area of blue–purple light emission.

Electrical properties were studied using the technique of impedance alternative spectroscopy over a temperature range 423–623 K in the frequency range of 40 Hz–13 MHz; conductivity under variable regime σ_{ac} follows Jonscher's law. The conductivity σ_{dc} follows the Arrhenius law with an activation energy value too low (≈0.3 eV) and decreased with the rate of iron, indicating polaronic conduction.

The dielectric study showed high values of dielectric constant at low frequency with low loss at high frequency. The modulus revealed dipolar relaxations.

* *Corresponding author.*
E-mail address: sdirinasr@yahoo.fr (N. Sdiri).
https://doi.org/10.1016/j.bsecv.2020.02.001

Efectos de la sustitución de Fe_2O_3 por K_2O en las propiedades físicas de los vidrios $88P_2O_5$–xFe_2O_3–2CoO–$(10-x)K_2O$

Palabras clave:
Vidrios
Calorimetría
Histéresis
Energía del intervalo
Espectroscopia de impedancia
Módulo

RESUMEN

Se prepararon vidrios $88P_2O_5$–xFe_2O_3–2CoO–$(10-x)K_2O$ de $x=0{,}0$ a $x=0{,}5$ a 850 °C con la técnica de enfriamiento rápido *(melt quenching)*.

Estos sistemas vítreos se caracterizaron por el uso de difracción de rayos X, calorimetría diferencial de barrido (DSC), mediciones magnéticas, espectroscopia Raman, métodos de Arquímedes, espectrómetro Brewster, espectrofotómetro UV-Vis y espectroscopia de impedancia. La difracción de rayos X reveló que estos sistemas vítreos tienen una estructura amorfa. La DSC ha demostrado que la estabilidad térmica de las muestras de vidrio aumentó con la tasa de hierro. Los espectros Raman mostraron la existencia del grupo PO-Fe que incrementa la rigidez de las muestras de vidrio. La densidad de nuestros compuestos se incrementó con el aumento de la cantidad de óxido de hierro.

Las mediciones magnéticas a 5 K utilizando la técnica del magnetómetro de muestra vibracional muestran el comportamiento antiferromagnético de estos vidrios del sistema.

De acuerdo con los resultados de los espectros de absorción óptica, los valores de la energía del intervalo y la energía de Urbach disminuyeron, y el índice de refracción del vidrio aumentó con el aumento del mol de Fe_2O_3. El espectrofotómetro Brewster ha mostrado un índice óptico ($n>1{,}5$). En cambio, las coordenadas cromáticas de todas las muestras al área de emisión de luz azul-púrpura.

Las propiedades eléctricas se estudiaron utilizando la técnica de espectroscopia alternativa de impedancia en un rango de temperatura de 423-623 K en el rango de frecuencia de 40 Hz-13 MHz; la conductividad por el régimen variable σ AC sigue la ley de Jonscher. La conductividad σ_{dc} sigue la ley de Arrhenius con un valor de energía de activación demasiado bajo ($\approx 0{,}3$ eV) y disminuía con la tasa de hierro, lo que indica conducción polarónica.

El estudio dieléctrico mostró valores altos de constante dieléctrica a baja frecuencia con baja pérdida a alta frecuencia. El módulo reveló relajaciones dipolares.

Introduction

Many scientific applications have recently been interested in the study of oxide glasses [1]. The glasses formed by Fe_2O_3–P_2O_5 are very useful in practice, for scientific reasons because they are considered a matrix of large capacity for the storage of nuclear waste [2]. P_2O_5 represents an archetypal glass former. In fact, this phosphate glass is used in many applications such as biocompatible materials for medical applications or lithium phosphate fast ion drivers that are used as electrolytes in the solid-state [3]. In addition, the iron reinforces the chemical bonds in the phosphate glass structure, giving this glass comparable property, even better than borosilicate glasses [4].

Phosphate glasses are generally easy to prepare and have a wide variety of applications in optics, electrical and solid states batteries technology, due to their high coefficient of thermal expansion, low transition temperature and high electrical conductivity [5,6]. Moreover, Phosphate-based glasses are nowadays studied because they are useful in the biomaterial fields [7]. A lot of theoretical researches on phosphate glasses have established that the glassy P_2O_5 lattice is formed from PO_4 tetrahedra, which are connected by P–O–P bonds forming a polymer structure [8]. The problem with simple phosphate glasses is that they do not have high chemical stability. It is now known that the addition of transition metals, such as iron and/or bismuth increases the aqueous stability of phosphate glasses by the formation of P–O–Fe and/or P–O–Bi bond [9]. Iron exists in glass, frequently in two valence states, Fe^{3+} and Fe^{2+} [10,11].

The addition of a modifying oxide (generally alkaline or alkaline earth) changes the characteristics of the three-dimensional random lattice to one of the linear phosphate chains. In terms of the terminology Q^n (where n is the number of oxygen atoms bridged by PO_4 tetrahedron), the effect of the modifying oxide concentration on the phosphate structural groups is the shift from the ultra-phosphate Q^3 ($[P(OP)_3(OP–)_1]$) to meta-phosphate Q^2 ($[P(OP)_2(OP–)_2]$) to pyrophosphate Q^1 ($[P(OP)(OP–)_3]$). The infinitely long phosphate chains are shortened; hence the induction of a break in the coherence of the network and the formation of non-binding oxygen groups (NBO) [12].

Recently, a research [13] has shown that the insertion of high amount of transition metal (TM) in alkaline phosphate glasses induces conductivity anomalies. Such anomalies result from the fact that the negatively charged polarons interact with mobile (alkali) cations to form uncharged diffusing entities minimizing conductivity, the so-called “ion-polaron effect” [14].

The glass-making techniques most commonly used in glass research are melt quenching, chemical vapor deposition

and sol-gel methods. In fact, the melt quenching technique was the oldest glass preparation technique used in the glass industry as well as in the research field, before chemical vapor deposition and sol-gel technique.

The melt quenching technique is characterized by its flexibility in the preparation of a large number of glass compositions of silicate, borate, phosphate, oxide or non-oxide systems.

Among the advantages of this method, the doping or co-doping of different types of active ions is quite easy. Compared to other glass preparation methods, the disadvantage is the lack of purity of the prepared glass sample. In order to avoid any contamination, the crucibles made of noble metals such as gold, platinum, etc. can be used.

In our work, bulk glasses were prepared using a melt quenching method; we chose oxide phosphate as glasses network formers. Indeed, phosphate glasses with a high amount in glass have several advantages. They are characterized by their high coefficient of thermal expansion, ultraviolet transmission, low melting temperatures and high electrical conductivity [15–17].

Cobalt ions are expected to have profound influence on the physical properties of glasses, as they exist in different valance states viz., Co^{2+}, Co^{3+} and Co^{4+} states [18] and they have a high value of optical index, which allows them to be good candidates for nonlinear optics [19].

On the Other hand, we have added to our glass samples an alkali metal (K^+) that increases the concentration of non-bridging oxygen and decreases the melting temperature.

To our knowledge, the use of these two metals together with small proportions has not been addressed in the literature.

Therefore, in order to reinforce the polaron conduction in front of the ionic conduction, increase the thermal, chemical stability and increases the optical index of our glass we have chosen to add cobalt in the presence of iron. Moreover, we have added cobalt and iron ions with low concentration to avoid conductivity anomalies [13,20].

The modulus formalism has the advantage of extracting the dielectric response of bulk at high frequencies by masking the relaxation that results from the conduction and by removing the polarization of the electrodes [21,22].

For electrical and dielectric measurements, we chose to use impedance spectroscopy given that this technique is powerful in probing glass materials.

In this work, we study the variation of the physical, structural, thermal, optical, electrical, dielectric and magnetic properties of glass samples with low iron content.

Experiment

Glass preparation

The samples used for the manufacture of glass, with the molar formula $88P_2O_5$–xFe_2O_3–2CoO–$(10-x)K_2O$ were prepared from high purity chemicals (99.99%): $(NaH_2PO_4)2H_2O$, Fe_2O_3, K_2O and CoO anhydrous. Suitable amounts of the raw materials were crushed, dosed and mixed, each time about 10 g is weighed and then placed in a heated platinum furnace crucible for 30 mn to remove impurities in the form of gas. They were, then, melted at 1023 K in a high temperature oven. After heating, the melt was poured at room temperature into a preheated graphite mold (at 200 °C). Subsequently they were quenched and annealed at about 200 °C in a muffle furnace. The obtained glasses were cut into granules, which have the shape of a disk with $R = 3.5$ mm radius and $e = 2.5$ mm thickness and then polished for the optical measurements of the spectra. The batches of each glass composition (in mol%) are given in Table 1.

Table 1 – Glass codes, glass composition (in mol%) and molar mass (M) (g/mol).

Glass code	Composition	M (g/mol)
PCKF00	$88P_2O_5$–2CoO–$10K_2O$	135.88
PCKF01	$88P_2O_5$–$0.1Fe_2O_3$–2CoO–$9.9K_2O$	135.94
PCKF02	$88P_2O_5$–$0.2Fe_2O_3$–2CoO–$9.8K_2O$	136.01
PCKF03	$88P_2O_5$–$0.3Fe_2O_3$–2CoO–$9.7K_2O$	136.07
PCKF04	$88P_2O_5$–$0.4Fe_2O_3$–2CoO–$9.6K_2O$	136.14
PCKF05	$88P_2O_5$–$0.5Fe_2O_3$–2CoO–$9.5K_2O$	136.18

Technical measurements

The phosphate Glass powder samples obtained by grinding the glass were used for XRD characterization. The XRD diagram of the samples was recorded using a Philips X'Pert X-ray diffractometer, which uses Cu-Kα radiation ($\lambda = 1.54056$ Å) at 40 kV and 100 mA and setting the diffractometer in the 2θ interval from a weak angle of 5° to 70° by changing the 2θ with a step of 0.02°.

Raman measurements were carried out using a visible LabRAM HR spectrometer (Horiba Gr, France) with a wavelength excitation of 632.8 nm emitted from He–Ne laser.

Using Archimedes' method, and using acetone as immersion liquid, we measured the density ρ of each glass. The glass discs were weighed in the air (Wair) using an electronic scale, (±0.01 g) were manufactured by Melter Toledo, and then immersed in acetone and reweighed (ω_{ac}). The density of acetone $\rho_{ac} = 0.789\ g\,cm^3$.

The refractive index was measured using the Brewster angle method with Laser He–Ne at 25 °C.

DSC (Differential Scanning Calorimetry) scans of gas-cast glass specimens were carried out in Toledo DSC823e Instruments. The DSC scans were recorded using 4 gas-cast glass specimens. These were powdered and heated with heating rates of 10 °C/min between 20 and 450 °C temperatures in a platinum crucible using the same amount of alumina powder as reference material.

5 K temperature measurements of the magnetization as the H-field were recorded using a vibrating sample magnetometer. This measurement was taken in the magnetic field (H) −10 to 10 T range.

To understand the optical absorption coefficient $\alpha(\lambda)$ of the polished samples, the diffuse reflectance spectra in the UV–visible region were made at room temperature by using a Shimadzu UV-2501PC spectrophotometer.

Complex impedance data of disk-shaped samples such as diameter ($d = 7$ mm) and thickness ($e = 2$ mm) were analyzed using an impedance analyzer (Agilent 4294 A) in the frequency

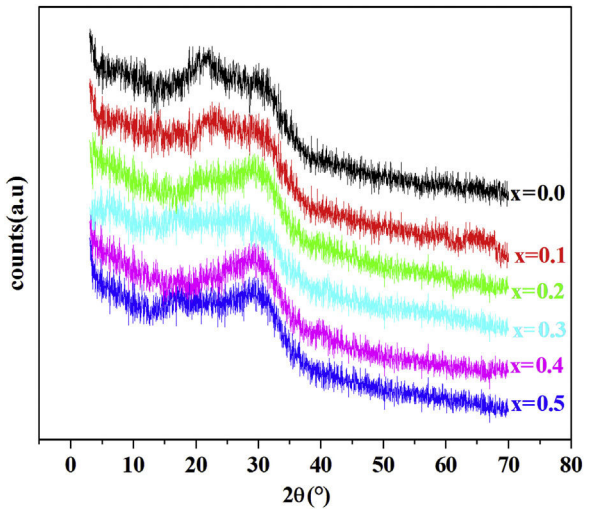

Fig. 1 – XRD patterns of PFCK00, PFCK01, PFCK02, PFCK03, PFCK04 and PFCK05 glasses at room temperature.

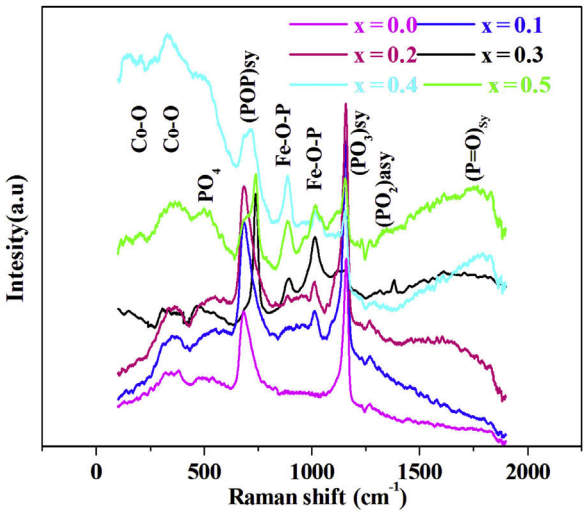

Fig. 2 – Raman spectra of PFCK00, PFCK01, PFCK02, PFCK03, PFCK04 and PFCK05 glasses at room temperature.

range from 40 Hz to 107 Hz and in a 423–623 K temperature range.

Results and discussion

XRD result

Fig. 1 shows the XRD patterns of PFCK00- PFCK05 glasses at room temperature. In this diffractogram there are a wide scattering ranging between $2\theta = 12°–35°$ and the absence of a sharp crystallization peaks which is characteristic of the amorphous phase.

Raman spectroscopy

The Raman spectra for series of $88P_2O_5–xFe_2O_3–2CoO–(10-x)K_2O$, from $x = 0.0$ to $x = 0.5$, glasses are given by Fig. 2.

In the 150–2000 cm^{-1} spectral range, the Raman spectrum reveals the band spectral 160–198 cm^{-1} assigned to CoO [23], the band at 470 cm^{-1} associated to PO_4 bending mode in Q^0 [24]. The band at around 690 cm^{-1} is due to the motion of bridging oxygen $(P–O–P)_{sym}$ in Q^2 [25], the band at 900 and 1000 cm^{-1} is assigned to symmetric and asymmetric vibrations of the Fe–O–P [25]. The intense peak located at 1170 cm^{-1} is attributed to the symmetric stretching mode of non-bridging $(PO_3)_{sym}$ [26]. The band at around 1270 cm^{-1} is related to stretching vibrations $(PO_2)_{sym}$ [27]. The high frequency band at around 1300 cm^{-1} is due to $(P{=}O)_{sym}$ stretch mode [24].

Physical parameters

For the measurement of the density ρ of each glass, the Archimedes method was used with acetone as the immersion liquid. The glass disk was weighed in the air (Wair) using an electronic scale, (±0.01 g) manufactured by Melter Toledo, and immersed in acetone and reweighed (ω_{ac}), the density of acetone $\rho_{ac} = 0.789\ g\,cm^{-3}$, the relative density is given by the following formula [28]:

$$\rho = \rho_{ac}\frac{\omega_{Air}}{\omega_{ac}} \quad (1)$$

For measurement of the refractive index, the method of Brewster angle with Laser He–Ne at 25 °C was used.

To calculate the molar refraction, R_m, of our samples, we used the well-known formula of Volf and Lorentz–Lorenz [29]:

$$R_m = \frac{n^2-1}{n^2+2}\frac{M}{\rho} \quad (2)$$

Table 2, summarizes all the physical characteristics of our samples: density (ρ), molar mass of the compound (M), molar refraction, R_m and the refractive index (n).

From Table 2 it can be seen that as the Fe_2O_3 content increases, the molar volume of the glasses decreases. The observed decrease of V_m indicates the implantation of the coordination polyhedra in the structural network [31]. The result induces a very slight variation in molar refraction, R_m observed in Table 2. In fact, molar refraction is an electronic polarizability per mole and it includes contributions from each component of mixture [32].

DSC results

The Differential Scanning Calorimetry (DSC) data Fig. 3 of PFCK00-PFCK05 glasses showed transitions (T_g) in the 120–140 °C temperature range. When the temperature exceeds T_g, the atoms can migrate relatively to each other. We reach a temperature at which the atomic rearrangement becomes possible and the glass crystallizes. This phenomenon is exothermic, T_x denotes the crystallization start temperature which varies between 270 and 300 °C. The difference between the crystallization temperature and the glass transition temperature ($T = T_x - T_g$) gives information about the stability of

Table 2 – Density (ρ), molar volume (V_m), molar refraction, R_m and the refractive index (n) of the glass systems $(90-x)P_2O_5$–xFe_2O_3–5CoO–$5K_2O$ for $x = 0.0$, 0.1, 0.2, 0.3, 0.4 and 0.5 compared with other work.

Glass code	ρ (g/cm^3)	V_m (cm^3/mol)	R_m (cm^3/mol)	Refractive index, n	Ref
PCKF00	2.43	55.91	29.57	2.09	–
PCKF01	2.48	54.81	29.48	2.12	–
PCKF02	2.51	54.18	29.79	2.16	–
PCKF03	2.58	52.74	29.30	2.18	–
PCKF04	2.62	51.96	29.31	2.21	–
PCKF05	2.73	49.88	33.42	2.25	–
$(P_2O_5)_{65}(ZnO)_5(MoO_3)_{20} + (Na_2O)_5\ (Al_2O_3)_5$	2.78	43.17	23.92	1.68	[30]

Table 3 – Thermal parameters of PCKF00, PCKF01, PCKF02, PCKF03, PCKF04 and PCKF05 compared with other glass.

Samples	T_g (°C)	T_x (°C)	$\Delta T = T_x - T_g$ (°C)	Ref.
PCKF00	127.57	264.23	136.66	Our work
PCKF01	127.57	265.26	137.69	–
PCKF02	127.57	266.34	138.77	–
PCKF03	127.57	266.54	138.97	–
PCKF04	122.82	301.41	178.59	–
PCKF05	122.81	306.16	183.35	–
$(P_2O_5)_{50}(CaO)_{20}(SrO)_{20}(Na2O)_{10}$	436.00	550.00	114	[34]

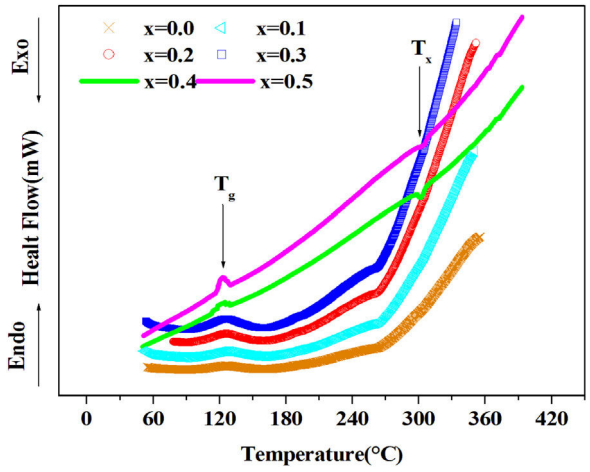

Fig. 3 – DSC curves of PFCK00, PFCK01, PFCK02, PFCK03, PFCK04 and PFCK05 glasses with heating rates of 10 °C/min; the temperature precision was ±1 °C.

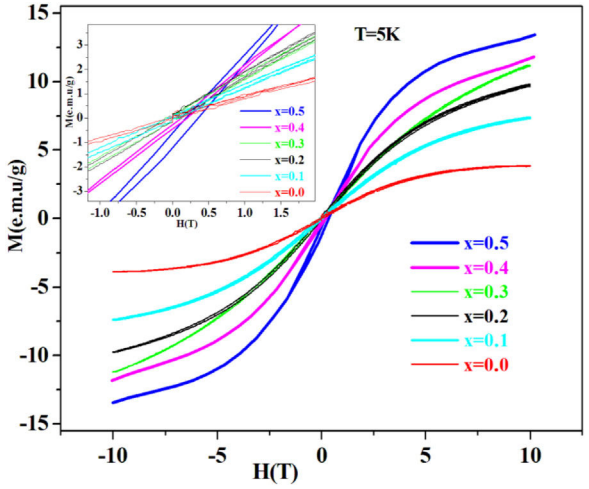

Fig. 4 – *M–H* loops of PFCK00, PFCK01, PFCK02, PFCK03, PFCK04 and PFCK05 glasses at 5 K temperature, Insets show enlarged view of *M–H* loops near the origin.

the glass [33]. The ΔT values corresponding to our samples are gathered in Table 3.

From Table 3 it can be seen that ΔT increases with Fe_2O_3 content and is above 100 °C, indicating that our samples are thermally stable and have better chemical durability.

The good chemical durability of iron phosphate glass is due to a large number of Fe–O–P bonds in the structure [35].

Magnetic study

As shown in Fig. 4. PFCK00-PFCK05 glasses show antiferromagnetic behavior, with obvious hysteresis loops. Also, it is found out that the magnetization saturation phenomenon increases Fe_2O_3 content.

The coercive field and the low remanent magnetization are viewed in the inset in Fig. 4, where an expanded view around the central part of the hysteresis cycles is shown. It can be seen that the low area hysteresis cycles increase with the increase of mol% of Fe_2O_3. The magnetic behavior observed is similar to that of soft magnetic materials with narrow hysteresis loop and low coercivity.

Optical study

The absorption coefficient $\alpha(\lambda)$ for PCKF00-PCKF05 was calculated from the relation [36]

$$\alpha(\lambda) \equiv \frac{(1-R_\infty)^2}{2R_\infty} \tag{3}$$

R_∞ is the diffuse reflectance of the powder sample.

Fig. 5 shows the UV–visible absorption (α) spectra of Fe_2O_3 doped glasses PFCK00-PFCK05. This figure reveals peaks

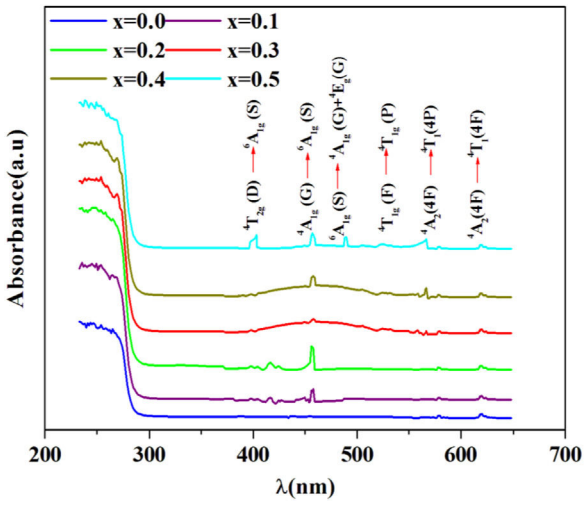

Fig. 5 – α, optical absorbance spectra of PFCK00, PFCK01, PFCK02, PFCK03, PFCK04 and PFCK05 glasses at room temperature.

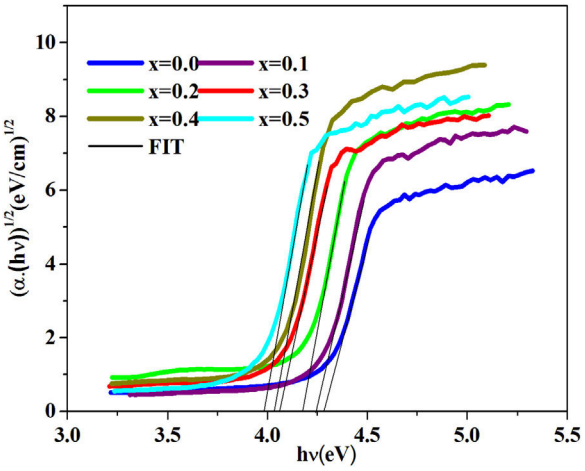

Fig. 6 – $(\alpha\nu)^{1/2}$ versus $(h\nu)$ plot for PFCK00, PFCK01, PFCK02, PFCK03, PFCK04 and PFCK05 glasses.

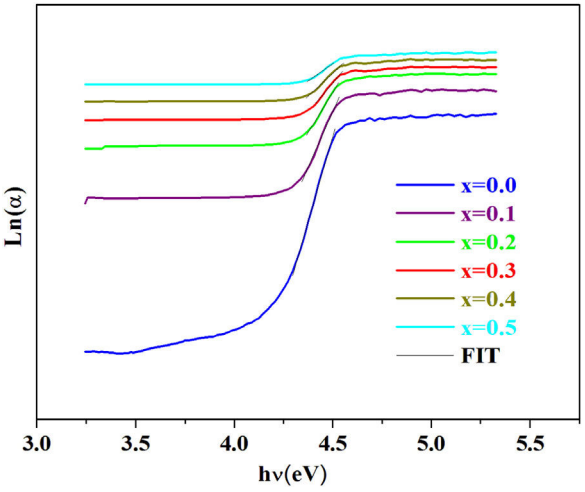

Fig. 7 – The Urbach plots of (PFCK00, PFCK01, PFCK02, PFCK03, PFCK04 and PFCK05) samples.

appearing between 400 and 700 nm which correspond to the absorption of iron and cobalt [37,38].

The large absorption bands original from the d–d transition of metal transition ions is observed. In fact this domain is assigned to charge transfer.

For $x = 0$, there are three weak UV absorption bands at about 530, 575, and 620 nm, which are assigned to the transitions $^4T_{1g}(F) \rightarrow {}^4T_{1g}(H)$, $^4A_2(4F) \rightarrow {}^4T_1(4P)$ and $^4A_2(4F) \rightarrow {}^4T_1(4F)$, respectively which caused by cobalt emission [39].

By introducing Fe_2O_3, there are three peaks located at about 248, 373, 448 and 455 nm which are associated with the transitions $^6A_{1g}(G) \rightarrow {}^4T_{2g}(D)$, $^4T_{2g}(D) \rightarrow {}^6A_{1g}(S)$, $^4A_{1g}(G) \rightarrow {}^6A_{1g}(S)$ and $^6A_{1g}(S) \rightarrow {}^4A_{1g}(G) + {}^4E_g(G)$, respectively [40,41].

To calculate the values of the optical band gap, optical data was analyzed using Tauc's law [42]:

$$(\alpha h\nu) = B(h\nu - E_g)^p \tag{4}$$

where B is a band constant, E_g is the energy of the optical band gap and p factor depends on the type of transition and the structures of the material. In the case of an amorphous phase, indirect transitions ($p = 2$) [43] are the most frequent.

Plotting $(\alpha h\nu)^{0.5}$ as a function of photon energy $h\nu$, Fig. 6, the indirect gap, E_g was determined by extrapolating the linear segment of the curve to the $h\nu$ axis where $(\alpha h\nu)^{0.5} = 0$.

To estimate the Urbach energy or band tail width (E_u) one should apply Urbach relation:

$$\alpha = \alpha_0 \, e^{h\nu/E_u} \tag{5}$$

where α_0 is constant and E_u represents the width of the band tail of the states in the forbidden band and indicates the degree of disorder in the materials [44].

The values of the Urbach energy (E_u) of our glasses are determined by taking the reciprocal values of the slopes of the linear part of the ln(α) vs $h\nu$ plots, as shown in Fig. 7.

The optical energy gap (E_{gt}) of the samples is theoretically calculated from the refractive index values (n) measured using the relationship given by Dimitrov and Sakka [45]:

$$E_{gt} = 20 \times \left(1 - \frac{n^2 - 1}{n^2 + 2}\right)^2 \tag{6}$$

The band gap energies (E_g), Urbach energy (E_u) and the band gap (E_{gt}) are presented in Table 5.

Table 4 shows that as the amount of iron increases the band gap decreases. The decrease in the optical gap E_g could be attributed to structural differences of the network caused by the increase of the rate iron. This result was observed by Gúth et al. [47] and Elbashar et al. [48]. Consequently, the different ionic states improve the concentration of non-bridging oxygens (NBOs) and the states from the NBO are better excited easily than those of the bridged oxygen atoms. And then, the increase in the concentration of NBO ions induces the displacement of the valence band toward higher energies and

Table 4 – The dissolution rate of glasses and the molar ratio of iron ions $R = Fe^{2+}/Fe^{3+}$.

	Samples				
	PCKF01	PCKF02	PCKF03	PCKF04	PCKF05
The dissolution rate (10^{-7} g/cm^2 min)	24.338	19.846	13.892	9.569	3.138
$R = Fe^{2+}/Fe^{3+}$	0.26	0.24	0.21	0.18	0.15

Table 5 – Gap energy, E_g, gap energy theoretical, E_{gt} and Urbuch energy, E_u values for different compositions of glasses.

Glasses	E_g (eV)	E_{gt} (eV)	E_u (eV)	Ref
PCKF00	4.31	4.42	0.08	Our work
PCKF01	4.23	4.27	0.11	–
PCKF02	4.14	4.19	0.16	–
PCKF03	4.05	4.11	0.22	–
PCKF04	3.99	3.89	0.29	–
PCKF05	3.91	3.84	0.36	–
$(P_2O_5)_{40}(ZnO)_{40}(Na_2O)_{17}(MnO)_3$	3.86		0.47	[46]

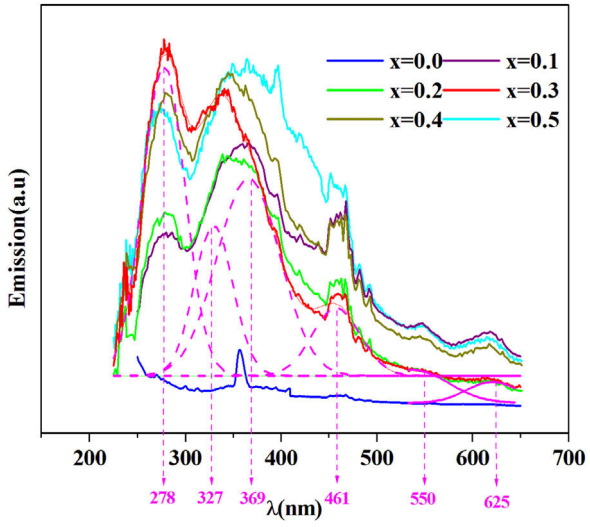

Fig. 8 – Emission spectra of PFCK00, PFCK01, PFCK02, PFCK03, PFCK04 and PFCK05 samples.

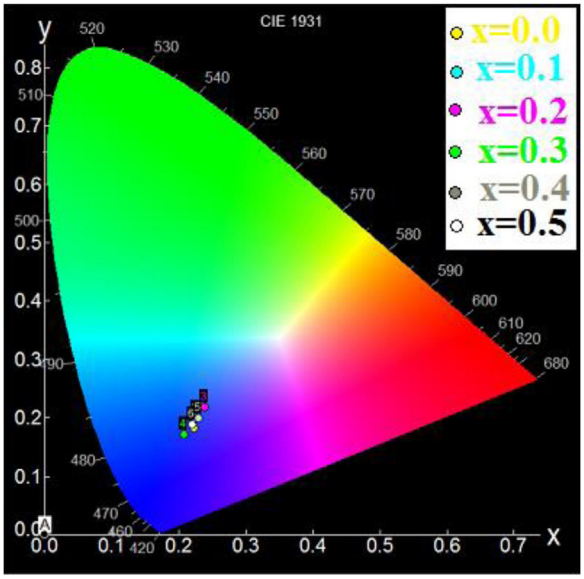

Fig. 9 – Location of the chromatic coordinates of the light emitted by: PFCK00, PFCK01, PFCK02, PFCK03, PFCK04 and PFCK05 samples.

decreases the energy of the band gap [49,50]. According to Table 4, we note that the optical gap values determined by the calculation are very close to the energy of the experimental gap.

The bad links and the fluctuations distorting angle bonds after the addition of iron are at the origin of defects, which explains the increase of the Urbach energy [51].

The emission spectra of the investigated samples were obtained using UV excitation with a wavelength of 220 nm at room temperature as given in Fig. 8.

From this figure, six principal emission bands are located at 278, 327, 369 (purple), 461 (blue), 550 (green) and 625 (red) with nm unit.

It can be seen from this spectrum that the emissions intensity increases overall with the amount of iron. Prabitha et al. [52] have observed the same result in the amorphous system TiO_2:Fe (0.8 and 1.1%).

Using the chromaticity diagram presented by CIELab [53], the chromaticity coordinates (x, y) are determined from the emission spectra to evaluate the performance of the materials. The CIELab chromaticity diagrams for all samples with 215 nm excitation wavelengths are determined (Table 6).

The chromatic coordinates of all samples to the area of blue-purple light emission (Fig. 9).

In fact, the prevalence of blue light in our daily life has increased exponentially with the improved technical and economic performance of current telecommunications systems that use blue light-emitting devices such as computers and smartphones, also LED bulbs and compact fluorescent lamps with low energy consumption [54]. In addition, the blue light laser is useful for various applications [55].

In medicine, blue light is widely used for tooth bleaching and restoration procedures involving composite resin [56].

However, blue light affects our eyes and this is now corrected by blue light blocking glasses can help [57]

Table 6 – Chromatic (x, y) coordinates of the emission color of PCKF00, PCKF01, PCKF02, PCKF03, PCKF04 and PCKF05 at room temperature under excitation with 215 nm.

Glass	PCKF00	PCKF01	PCKF02	PCKF03	PCKF04	PCKF05
(x,y)	0.222;0.181	0.226;0.199	0.240;0.216	0.208;0.171	0.229;0.198	0.220;0.188

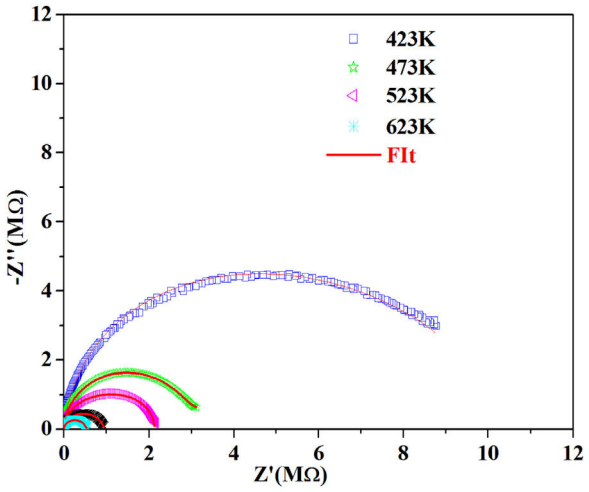

Fig. 10 – Experimental and theoretical impedance diagrams of the sample PFCK00 at different temperatures.

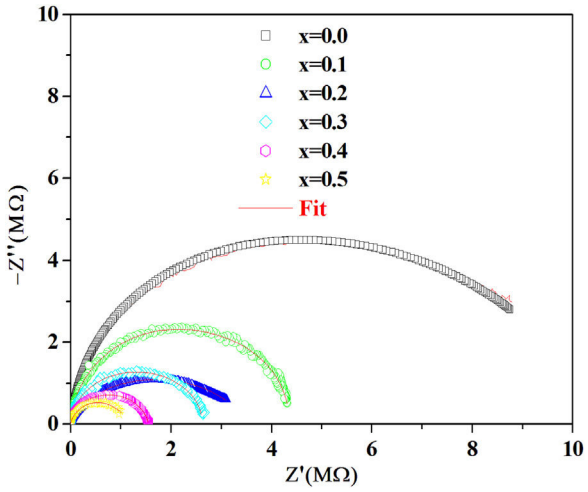

Fig. 11 – Experimental and theoretical impedance diagrams of the samples PFCK00, PFCK01, PFCK02, PFCK03, PFCK04 and PFCK05 at temperature T = 423 K.

Electrical study

Impedance spectra

Complex impedance spectroscopy (SIC) is a method of choice for describing qualitatively and quantitatively the mechanisms of conduction and dielectric relaxation in materials. For each frequency, the impedance complex, $Z^* = Z' + jZ''$ of the system is measured.

According to the complex impedance curves (Z'' vs. Z') of all the glass samples measured at 423 K and the PCKF00 sample at different temperatures (423–623 K) were found to have completed semicircles as shown in Figs. 10 and 11. It is observed that the complex impedance in the Nyquist diagram is represented in semicircular arcs whose centers are located under the Z' axis. However this behavior indicates the existence of a non-Debye relaxation for all samples [58]. Since the half circle is most often depressed, it is preferable to replace the capacitor with a constant phase element (CPE). Total impedance is given by:

$$Z* = Z' + jZ'' = \left[\frac{1}{R_b} + \frac{1}{Z*_{CPE}}\right]^{-1} \quad (9)$$

R_b is the bulk resistance we get with the cross of axis with the impedance curve [58].

The CPE impedance is defined by [58]:

$$Z*_{CPE} = \frac{1}{A_0(j\omega)^p} \quad (10)$$

where j is the imaginary unit ($j^2 = -1$), ω the angular frequency ($\omega = 2\pi f$, f is the frequency), A_0 a constant independent of frequency and p is a dimensionless parameter ranging between zero and unity and determining the degree of deviation from an exact semicircle [59].

In Eq. (10), depending on the value of p the CPE changes its behavior. For $p = 1$ The CPE has the behavior of an ideal capacitor such that $A = C$, for $p = 0$ the CPE behaves like a pure resistance such that $R = 1/A_0$.

With the software ORIGIN6.0 (Microcal Software, Inc., Northampton, MA, USA) these semicircles have been fitted according on the following relationships:

$$Z' = \frac{R_b(1 + R_b A_0 \omega^p \cos(p\pi/2)}{1 + 2R_b A_0 \omega^p \cos(p\pi/2) + (R_b A_0 \omega^p)^2} \quad (11)$$

$$Z'' = -\frac{R_b^2 A_0 \omega^p \sin(p\pi/2)}{1 + 2R_b A_0 \omega^p \cos(p\pi/2) + (R_b A_0 \omega^p)^2} \quad (12)$$

Fig. 10 shows that when iron concentration is fixed and the temperature increases, the real part impedance decreases. Thus, the glass conductivity improves. This result translates that electrical conduction is thermally activated in PFCK00 sample. On the other hand, from Fig. 11 we note that when the iron concentration increases the Z' impedance values decrease. Therefore, the samples conductivity improves. The results of the simulation are summarized in Table 7. R_b (bulk resistance) values decrease with increasing iron concentration. On the other hand, p values increase and approach 1 with iron concentration. This result makes relaxation tends toward the Debye type.

This behavior, which is related to the Raman spectrum for the glass samples Fig. 2, revealed that increasing the concentration of Fe_2O_3 in the glass network resulted in the formation

Table 7 – The best fitting values of equivalent circuit elements in different host materials at 523 K for PCKF00, PCKF01, PCKF02, PCKF03, PCKF04 and PCKF05 compared with $67B_2O_3$–23CaO–$10Li_2O$ (CaLiBO10).

Glass code	R_b (MΩ)	A_0 (10^{-11} F cm^2 s$^{\alpha-1}$)	α	Ref
PCKF00	0.611	1.345	0.743	Our work
PCKF01	0.432	1.675	0.792	–
PCKF02	0.386	2.023	0.824	–
PCKF03	0.319	2.542	0.886	–
PCKF04	0.244	3.132	0.931	–
PCKF05	0.212	3.876	0.989	–
CaLiBO10	60	1	0.925	[60]

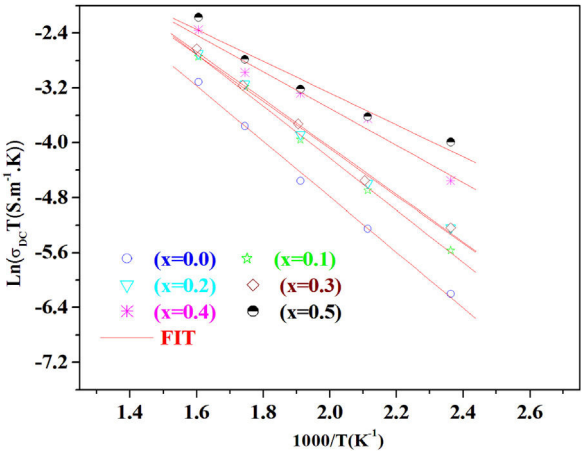

Fig. 12 – Variation of ln(σ_{dc}) versus 1000/*T* for PFCK00, PFCK01, PFCK02, PFCK03, PFCK04 and PFCK05 glasses.

of a large number of non-bridging sites. This behavior allows easy conduction of charge carriers which explains the increase in electrical conductivity thus observed [62].

DC conductivity

Phosphate glass has a broad distribution of permanent deficiencies likely to host some cations (or anions). Weak covalent network-related ions can migrate under the action of an electric potential gradient where the conductivity of a material results from the sum of its electronic and ionic conductivity. Thus, the conduction is entirely ensured by the ions that move under the action of an electric field. σ_{dc} is the dc conductivity of the sample and It is given by the following formula [54,59]:

$$\sigma_{dc} = \frac{e}{SZ_0} \tag{13}$$

where A is the sample area ($A = \pi d^2/4$), e is the sample thickness and Z_0, which is defined by the interception of the real axis with the lowest frequency curve.

The calculation of uncertainties on the dc conductivity, σ_{dc} are expressed by:

$$\Delta\sigma_{dc} = \sigma_{dc}\left(\frac{\Delta e}{e} + \frac{\Delta d}{d} + \frac{\Delta Z_0}{Z_0}\right) \tag{14}$$

The temperature dependence of conductivity for glass batches is measured. This is plotted in Fig. 12 as ln($\sigma_{dc}T$) versus the temperature. All the plots are linear, indicating that both DC conductivity and the hopping process exhibit a thermally activated behavior and obey Arrhenius law given by the equation:

$$\sigma_{dc}T = \sigma_0 \exp\left(\frac{-E_a}{K_BT}\right) \tag{15}$$

where E_a is dc activation energy, σ_0 is a pre exponential factor, T is the absolute temperature and K_B is the Boltzmann constant. E_a and σ_0 are parameters independent of the temperature when the material is in a stable state and undergoes no phase transformation. On the other hand, the dc conductivity exhibits one activation barrier in the high and low temperature regimes. The activation energy is calculated from the slope of the linear plot. Moreover, we have calculated the uncertainties on the activation energy E_a, as follows:

$$\Delta E_a = K_BT\left(\frac{\Delta\sigma_{dc}}{\sigma_{dc}} + \frac{\Delta T}{T}\left(1 + \frac{E_a}{K_BT}\right)\right) \tag{16}$$

with $\Delta T = \pm 0.01\,^{\circ}C$.

From Fig. 12, the graph shows that the conductivity of the glass sample decreases linearly with decreasing temperature. The activation energies corresponding to all iron compositions in the glass are listed and compared with $60P_2O_5$–$35V_2O_5$–5CuO glass in Table 8. According to Table 8, the activation energy value is low and its value decreases with Fe_2O_3 amount.

This result suggests a polaronic conduction between the iron and cobalt ion sites across the oxygen bridge. In phosphate glasses, iron ions exist as Fe^{3+} in both tetrahedral and octahedral coordination and as Fe^{2+} in octahedral environment [62,63].

Electrical conduction in these glasses occurs by electron hopping from an ion of low valence state (Fe^{2+},Co^{2+}) to an ion of the high valence state (Fe^{3+},Co^{3+}).

The highest value of the activation energy (E_a) is obtained for the glass sample PCKF0 and shows that the increase of Fe_2O_3 concentration, the ratio of transition metals Fe^{2+}/Fe^{3+} and the conductivity increases. So magnetism increases and electrical conduction too. A conduction mechanism is due to exchange interaction of Fe^{2+}–O–Fe^{3+} chains and it has been attributed to electron hopping between them.

AC conductivity

Fig. 13 shows the plot of σ_{ac} versus frequency at different temperatures for PFCK00 sample. The conductivity σ_{ac} is

Table 8 – Activation energy, E_a, values for different composition of glasses.

Glass	PCKF00	PCKF01	PCKF02	PCKF03	PCKF04	PCKF05	$60P_2O_5$–$35V_2O_5$–5CuO [61]
E_a (eV)	0.35	0.32	0.30	0.29	0.24	0.25	0.88

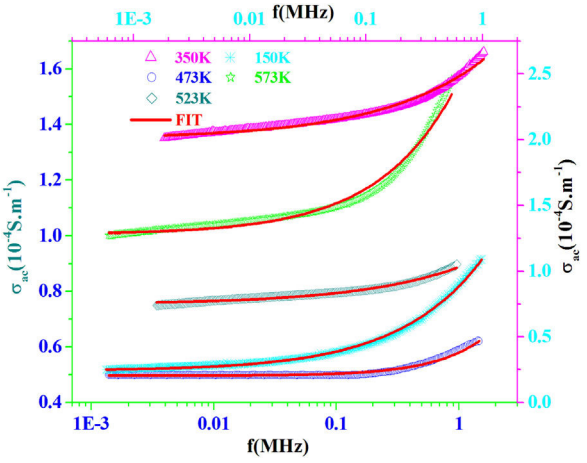

Fig. 13 – Variation of the ac conductivity versus frequency (*f*) of the sample PFCK00 at different temperatures.

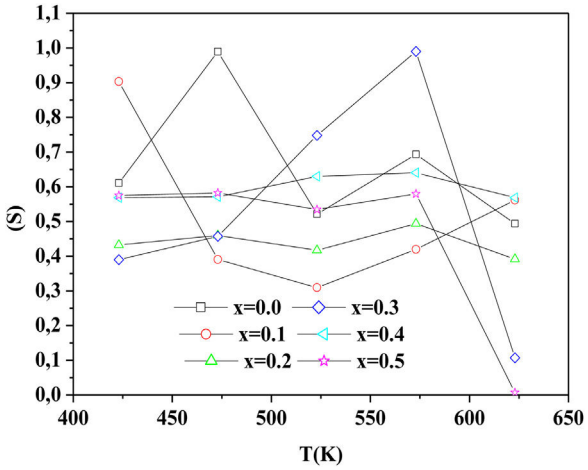

Fig. 14 – Variation of the exponent S with temperature for different samples.

calculated from the data of complex impedance values using the relation [64]:

$$\sigma_{ac} = \frac{e}{A}\frac{Z'}{(Z'^2 + Z''^2)} \tag{17}$$

where A is the area of the sample and *e* its thickness.

Conductivity is proportional to angular frequency in amorphous materials; it generally obeys Jonscher's law [65]:

$$\sigma = \sigma_{dc} + A\omega^{S(T)} \tag{18}$$

where σ_{dc} is the dc conductivity, ω is the angular frequency and $\sigma_{ac}(\omega) = A\omega^{S(T)}$ is the AC component. A is a constant for a particular temperature and S(T) is an exponent function of temperature and frequency. It is related to the degree of correlation among moving ions, generally with values between $0 < S < 1$. It is clear that two different regions are observed in Fig. 13.

At a lower frequency region ($\omega < 0.01$ kHz), the DC conductivity remains constant since there is a plateau (σ_{dc}) independent of the frequency.

At the higher frequency and temperature and obeying power law $\omega^{S(T)}$, the point at which the change in slope occurs is known as hopping frequency f_{hop} [66]. From f_{hop} we can calculate the hopping time τ_{hop} ($f_{hop} = 1/\tau_{hop}$). In the higher frequency region, the increase in conductivity is due to the hopping of charge carriers in finite clusters.

To determine the origin of the conduction mechanism, we studied the behavior of factor S as a function of temperature. S is calculated from the slopes of linear of the relation of log $\sigma_{ac} = f(\omega)$.

The variation of S with temperature for all samples is shown in Fig. 13.

Furthermore, various theoretical models were proposed to describe the predominant conduction mechanism under AC field.

According to Fig. 14, for the sample PCKF00, S exponent varies in an oscillatory way with the temperature. This result translates conduction by the small polaron tunneling model (SPT) if S increases [67] and by the correlated barrier hopping (CBH) conduction mechanism if S decreases [68]. In fact, (SPT) and (CBH) models are, respectively described by the following equations [63,68]:

$$S = 1 - \frac{4}{\ln(1/\omega\tau_0) - W_H/k_BT} \tag{19}$$

$$S = 1 - \frac{6k_BT}{W_M - k_BT\ln(1/\omega\tau_0)} \tag{20}$$

where W_H is the activation energy, W_M is the binding energy, and k_B (86.17 μeV K^{-1}) is Boltzmann's constant, *T* is the temperature and τ_0 is the relaxation time.

For the samples PCKF02, PCKF04 and for PCKF05 in the range of 425–575 K, the exponent S remained moderately unchanged with the temperature. The result has mostly assumed that carrier motion occurs through quantum mechanical tunneling (QMT) between localized states near the Fermi level [69,70]. However, for PCKF05, S decreases between 575 K and 625 K. This behavior is explained by (CBH) conduction mechanism.

For (QMT) model, frequency exponent is given by the following equation [69,70]:

$$S = 1 - \frac{4}{\ln(1/\omega\tau_0)} \tag{21}$$

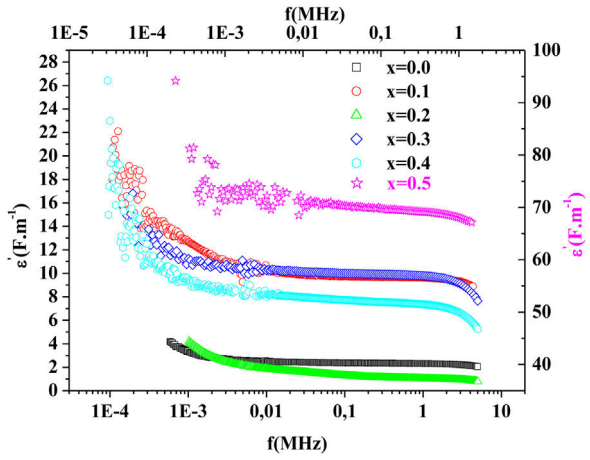

Fig. 15 – The frequency dependence curves of dielectric constant conduction ε' of PFCK samples at temperature T = 423 K.

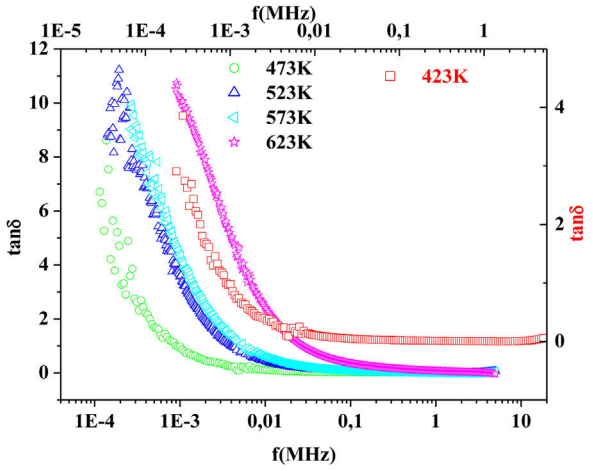

Fig. 16 – Variation of loss (tan δ), versus frequency for PFCK05 sample at different temperatures.

where ω is frequency and τ_0 is the atomic vibration period, $\tau_0 = 10^{-13}$ s.

For the sample PCKF01, the exponent S decreases to a minimum value and then increases. This behavior is assigned to the OLPT model [71]. In the case, the frequency exponent S is given by [71]:

$$S = 1 - \frac{8\chi R_\omega + (6W_{HO}r_p/R_\omega k_B T)}{\left[2\chi R_\omega + (W_{HO}r_p/R_\omega k_B T)\right]^2} \quad (22)$$

where W_{HO} the activation energy, r_p is the polaron radius, X is inverse localization length, R_ω is the hopping length at angular frequency, ω, r_p (is the tunneling distance), k_B is the Boltzmann constant and T is temperature.

For the sample PCKF03, the exponent S increases to a maximum value and then decreases with temperature. Thus, the electrical conduction is governed by (SPT) model if $T < 550$ K and by (CBH) if $T > 550$ K.

Dielectric study

We have determined different dielectric material parameters, from the measured resistive (real part Z′) and reactive (imaginary part Z″) of complex impedance at room temperature.

Dielectric constant (ε′) and dielectric loss (tan δ)

Dielectric constant ε' and loss tan δ were calculated using the following expressions [72]

$$\varepsilon' = \frac{-Z'}{\omega C_0 \left(Z'^2 + Z''^2\right)} \quad (23)$$

$$\tan\delta = \frac{Z'}{Z''} \quad (24)$$

Fig. 15 illustrates the variation of dielectric constant ε' for PFCK00-PFCK05 at 423 K as a function of frequency f.

For all samples, the dielectric constant ε' was relatively high at low frequencies, then it decreases sharply with frequency and remains almost constant over the entire frequency range.

On the other hand, for the PFCK05 sample, dielectric constant ε' had high values at low as well as at high frequency. In addition, for this sample there was low loss, tan δ (Fig. 16). This result allows PFCK05 to be a good candidate for application in the fields of electromagnetic wave guided in optical fibers, nonlinear optics, and in giant memory devices [73].

Modulus study

Modulus formalism is used to study the bulk spectral effects, when the resistances of the samples are comparable and their capacitances are different.

On the other hand, modulus formalism makes it possible to suppress the electrode effects [74,75].

Electric modulus is defined as [72]:

$$M*(\omega) = M'(\omega) + jM''(\omega) \quad (25)$$

where:

$$M'(\omega) = \omega C_0 Z'' \quad (26)$$

and

$$M''(\omega) = \omega C_0 Z' \quad (27)$$

Fig. 17 shows that M' values tends to zero at all the temperatures under study, suggesting the suppression of the electrode polarization [66]. At high frequency, M' tends to a maximum value, which translates the relaxation process.

By increasing the temperature, M' values increased. The result explains the dielectric and electrical thermal activation properties in PCKF05 glass. The dispersion observed at high frequencies in PFCK05 glasses may be attributed to the distribution of relaxation process.

The frequency dependence of M' and M'' at 423 K for PFCK00-PFCK05 glass are presented in Fig. 18. These figures clearly exhibit the relaxation character of dielectric properties of these glasses. Indeed, the maxima peak M''_{max} coincides with the inflection in the M' curve. On the other hand, the curves show that the value of M''_{max} shifted to lower

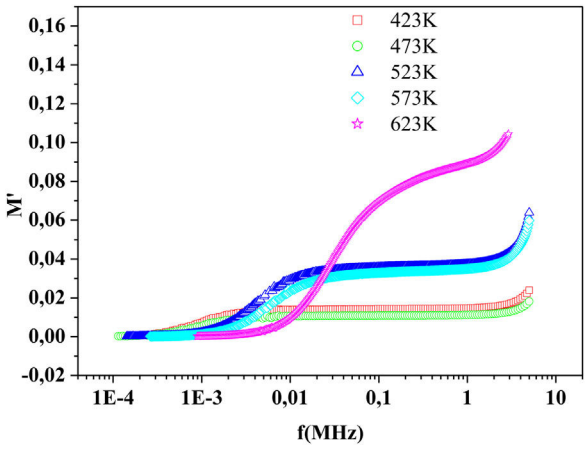

Fig. 17 – The frequency dependence of M′ for PFCK05 sample at different temperatures.

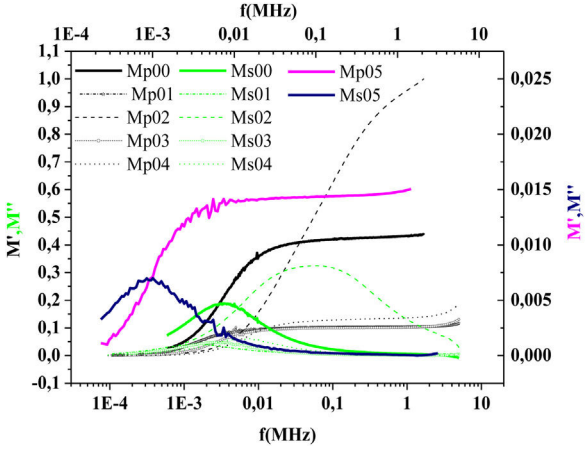

Fig. 18 – The frequency dependence of M″ and M′ for PFCK samples at temperature T = 423 K.

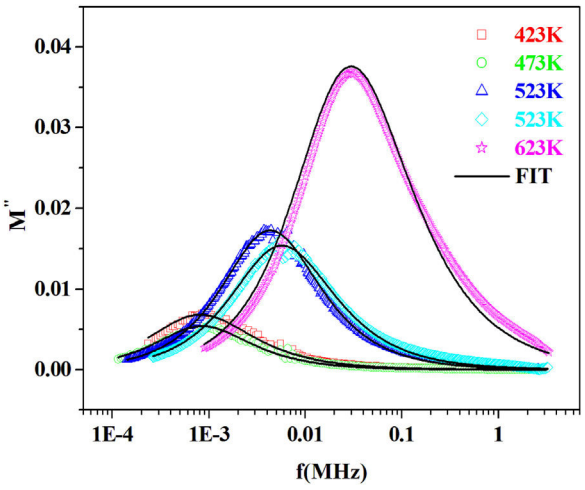

Fig. 19 – The frequency dependence of M″ for PFCK05 sample at different temperatures.

frequencies with Fe_2O_3 amount. For all samples, M'' curve showed a slight asymmetric peak. The frequency range below the peak frequency f_p determines the range in which charge carriers are mobile over long distances. At a frequency range above f_p, the carriers are confined to potential well being mobile over short distances [66].

The relaxation time τ_{rel} associated to each peak was calculated from the frequency at which the maxima of M'' occurs Table 9.

The values of Relaxation time, τ_{rel}, hopping time, τ_{hop}, of the prepared samples are listed in Table 8.

The variation of the imaginary part, M'' with frequency for the PFCK05 glass at different temperatures is presented in Fig. 19.

The electric modulus M^* could be expressed as the Fourier transform of a relaxation function $\varphi(t)$ [76]:

$$M* = M_\infty \left[1 - \int_0^\infty \left(\frac{-d\phi}{dt}\right) e^{-\omega t}\right] \quad (28)$$

where the function $\phi(t)$ is the time evolution of the electric field within the materials and is usually taken as the Kohlrausch–Williams–Watts (KWW) function [76]:

$$\phi(t) = e^{-(t/\tau_m)^\beta} \quad (29)$$

where τ_m is the conductivity relaxation time and the exponent $0 < \beta < 1$ indicates the deviation from Debye-type relaxation.

The electric modulus behavior of the present glass system is rationalized by invoking modified KWW function suggested by Bergman. The imaginary part of the electric modulus M'' is defined as [77]:

$$M'' = \frac{M''_{max}}{(1-\beta) + \frac{\beta}{1+\beta}\left[\beta\left(\frac{f_p}{f}\right) + \left(\frac{f}{f_p}\right)^\beta\right]} \quad (30)$$

where M''_{max} is the peak value of the M'' and f_p is the corresponding frequency.

The value of β could be determined by fitting the experimental data in the above Eq. (18).

The value of full width at half height (FWHH) of the imaginary part, M'' is calculated by equation [78]:

$$FWHH = \frac{1.14}{\beta} \quad (31)$$

From the fitting of the imaginary part of the modulus M'' versus frequency plots, the value of β is determined and found to be temperature-dependent. The plot of β and FWHH versus temperature is depicted in Fig. 20. β decreases gradually with the increase in temperature. Decreasing the value of β is an estimate of increased interaction between transition metals ((Fe^{2+}/Fe^{3+}), $((Co^{2+}/Co^{3+}))$ ions and surrounding matrix. Thus, coupling between mobile ions in the conduction process decreased. Therefore, this result favors the polaronic conduction in semiconductor materials.

On other hand, the shape of β is nearly constant below T_g. Then it decreased with increasing temperature above T_g. This behavior induces an incensement of FWHH parameter. This

Table 9 – Relaxation time, τ_{rel}, hopping time, τ_{hop}, for different compositions of glasses at 423 K.

Glasses	PCKF00	PCKF01	PCKF02	PCKF03	PCKF04	PCKF05
τ_{rel} (ms)	0.200	0.189	0.182	0.178	0.036	1
τ_{hop} (ms)	12.5	12.3	12.1	11.9	11.7	11.6

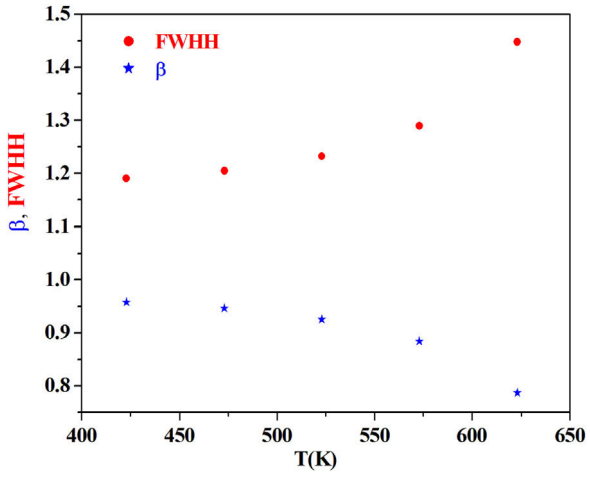

Fig. 20 – Variation of the exponent β with temperature for PFCK05 sample.

anomalous behavior of β can be explained by the fact that, above T_g, the system is in the supercooled liquid state and by the incurve of the degree of interaction of conducting ions [79].

Conclusion

Oxide phosphate glasses of the compositions $88P_2O_5$–xFe_2O_3–2CoO–$(10-x)K_2O$ from $x = 0.0$ to $x = 0.5$ [$x = 0.0$, 0.1, 0.2, 0.3, 0.4, 0.5] were prepared using melt-quenching technique. X-ray diffraction patterns show the presence of the amorphous state of the glass. Our glass has a good molar refraction and a refractive index which are 33.42 cm^3/mol and 2.1 respectively.

For the thermal properties of glass, we have found low values of transition temperature ($T_g = 1023$ K) for glass.

On the other hand, the increased ($T_x - T_g > 100$ °C) value with Fe_2O_3 amount reflects the stability of these glasses.

The P_2O_5–Fe_2O_3–FeO–BaO glasses reported here show particular promise as they are ultra-durable, thermally stable, low melting glasses with a large glass-forming compositional range.

On other hand, our glasses at 5 K have presented an antiferromagnetic behavior with narrow hysteresis loop and low coercivity.

Raman spectroscopy shows that the addition of Fe_2O_3 leads to the formation of Fe–O–P bonds.

Optical studies show that as the concentration of Fe_2O_3 increases the values of bandgap energy and Urbach energy decrease. On other hand, the band gap energy value of our glass is around 3.91 eV. The result, explains the behavior semiconductor in our samples.

Complex impedance plots for all compositions for showed the semicircular arcs are depressed and their centers lie below the Z′ axis, which suggests that the relaxation is of non-Debye type.

The conductivity $\ln(\sigma_{dc} \times T)$ versus $1000/T$ shows Arrhenius-type behavior. The d.c. electrical activation energy, $E_a = 0.3$ eV and decreased with increasing Fe_2O_3 concentration.

The ac conductivity followed Jonscher's law and the value of the power exponent (s) changed in composition.

The dielectric constant (ε') had considerable values especially at low frequencies with low dielectric losses, which had 28 F m^{-1} and 4 respectively.

In addition, our samples exhibit a low relaxation time, τ_{rel} and weak hopping time, τ_{hop} and which had 0.036 ms and 11.6 ms respectively. Furthermore, the dielectric data have been analyzed in modulus formalism using KWW stretched exponential function.

These results suggest that our glasses are a good candidates for semiconductor devices and electro-optical fiber-guided applications.

Acknowledgments

The authors thank FEDER funds through the COMPETE 2020 Program and National Funds through FCT – Portuguese Foundation for Science and Technology under the project UID/CTM/50025/2013.

REFERENCES

[1] T.V. Bocharova, G.O. Karapetan, A.M. Mironov, V.D. Khalilev, N.O. Tagil'tseva, Gamma induced absorption spectra as a new method for RE-ion environment study in a fluorophosphates glasses, Opt. Mater. 28 (2006) 1296–1300, http://dx.doi.org/10.1016/j.optmat.2006.02.015.

[2] W. Donald, Immobilisation of radioactive and non-radioactive wastes in glass-based systems: an overview, Glass Technol. 48 (2007) 155–163, http://pascal-francis.inist.fr/vibad/index.php?action=getRecordDetail&idt=19034815.

[3] R.K. Brow, the structure of simple phosphate glasses, J. Non-Cryst. Solids 28 (2000) 263–264, http://dx.doi.org/10.1016/S0022-3093(99)00620-1.

[4] Z. Chenkai, L. Jinsong, H. Songling, R. Chris, L. Xiaoling, The structure, degradation and fibre drawing properties of phosphate based glasses fibre: the effects of Fe_2O_3 and B_2O_3 addition, Ceram.-Silik. 62 (2018) 111–120, https://www.irsm.cas.cz/materialy/cs content/2018 doi/Zhu CS 2018 0002.pdf.

[5] S.M. Hsu, H.W. Yang, D.Y.C. Huang, W.L. Hsu, C.C. Lu, W.L. Chen, Development and physical characteristics of a novel compound radio photoluminescent glass, dosimeter, Radiat. Meas. 43 (2008) 538–541, http://dx.doi.org/10.1016/j.radmeas.2007.12.027.

[6] O. Cozar, D.A. Magdas, L. Nasdala, I. Ardelean, G. Damian, Raman spectroscopic study of some lead phosphate glasses

with tungsten ions, J. Non-Cryst. Solids 352 (2006) 3121–3125, http://dx.doi.org/10.1016/j.jnoncrysol.2006.03.066.
[7] S. Agathopoulos, D.U. Tulyaganov, J.M.G. Ventura, S. Kannan, M.A.J.M. Karakassides, F. Ferreira, Formation of hydroxyapatite onto glasses of the CaO–MgO–SiO_2 system with B_2O_3, Na_2O, CaF_2 and P_2O_5 additives, Biomaterials 27 (2006) 1832–1840, http://dx.doi.org/10.1016/j.biomaterials.2005.10.033.
[8] O. Cozar, D.A. Magdas, L. Nasdala, I. Ardelean, G. Damian, Raman spectroscopic study of some lead phosphate glasses ith tungsten ions, J. Non-Cryst. Solids 352 (2006) 3121–3125, http://dx.doi.org/10.1016/j.jnoncrysol.2006.03.066.
[9] L. Baia, R. Stefan, W. Kiefer, J. Popp, S. Simon, Structural investigations of copper doped B_2O_3–Bi_2O_3 glasses with high bismuth oxide content, J. Non-Cryst. Solids 303 (2002) 379–386, http://dx.doi.org/10.1016/S0022-3093(02)01042-6.
[10] C.S. Ray, X. Fang, M. Karabulut, G.K. Matasinghe, D.E.A. Day, Effect of melting temperature and time on iron valence and crystallization of iron phosphate glasses, J. Non-Cryst. Solids 249 (1) (1999), http://dx.doi.org/10.1016/S0022-3093(99)00304-X.
[11] M.D. Dyar, A review of Mossbauer data on inorganic glasses the effects of composition on iron valency and coordination, Am. Miner. 70 (1985) 304–316, https://pubs.geoscienceworld.org/msa/ammin/article-abstract/70/3-4/304/41717.
[12] G.S. Henderson, R.T. Amos, The structure of alkali germanophosphate glasses by Raman spectroscopy, J. Non-Cryst. Solids vol. 328 (2003) 1–19, http://dx.doi.org/10.1016/S0022-3093(03)00478-2.
[13] S.L. Kraevskii, U.F. Solonov, Ionic conductivity of glasses in the Me_nO_m–P_2O_5–M_2O systems and the effect of reduction in the percolation volume, Glass Phys. Chem. 32 (2006) 629, https://link.springer.com/article/10.1134/S1087659606030035.
[14] C.J. Bazan, J.A. Duffy, M.D. Ingram, M.R. Mallace, Conductivity anomalies in tungstate–phosphate glasses: evidence for an ion-polaron interaction, Solid State Ion 86–88 (1996) 497–501, http://dx.doi.org/10.1016/0167-2738(96)82669-5.
[15] M.R. Ahsan, M.G. Mortuza, Spectroscopic analysis of the effect of P_2O_5 in the 3:2 cadmium oxide silica glass, J. Phys. Chem. Glasses 42 (2001) 1–5, https://www.ingentaconnect.com/content/sgt/pcg/2001/00000042/00000001/4201001.
[16] R.K. Brow, The short-range structure of zinc polyphosphate glass, J. Non-Cryst. Solids 263–264 (2000) 1–28, http://dx.doi.org/10.1016/0022-3093(95)00289-8.
[17] Y.M. Mustafa, A. El-Adawy, Structural and physical properties of iron oxychloride phosphate glasses, Phys. Status Solid A 179 (2002) 83–93, https://doi.org/10.1002/1521-396X(200005)179:1<83::AID-PSSA83>3.0.CO;2-5.
[18] R.D. Shannon, Revised effective ionic radii and systematic studies of interatomic distances in halides and chalcogenides, Acta Crystallogr. A32 (1976) 751, http://dx.doi.org/10.1107/S0567739476001551.
[19] T. Satyanarayana, I.V. Kityk, M. Piasecki, P. Bragiel, M.G. Brik, Y. Gandhi, N. Veeraiah, Structural investigations on PbO–Sb_2O_3–B_2O_3–CoO glass ceramics by means of spectroscopic and dielectric studies, J. Phys. Condens. Matter 21 (2006) 245104, https://iopscience.iop.org/article/10.1088/0953-8984/21/24/245104/meta.
[20] X. Fang, C.S. Ray, A. Moguš-Milanković, D.E. Day, Iron redox equilibrium, structure, and properties of iron phosphate glasses, J. Non-Cryst. Solids 283 (2001) 162–172, http://dx.doi.org/10.1016/S0022-3093(01)00416-1.
[21] R. Ayouchi, D. Leinen, F. Martin, M. Gabas, E. Dalchiele, J.R. Ramos-Barrado, Preparation and characterization of transparent ZnO thin films obtained by spray pyrolysis, Thin Solid Films 426 (2003) 68–77, http://dx.doi.org/10.1016/S0040-6090(02)01331-7.
[22] B. Behera, P. Nayak, R.N.P. Choudhary, Study of complex impedance spectroscopic properties of $LiBa_2Nb_5O_{15}$, ceramics, Mater. Chem. Phys. 106 (2007) 193–197, http://dx.doi.org/10.1016/j.matchemphys.2007.05.036.
[23] N. Kornienko, J. Resasco, N. Becknell, C. Jiang, Y. Liu, K. Nie, X. Sun, J. Guo, S. Leone, P. Yang, Operando spectroscopic analysis of an amorphous cobalt sulfide hydrogen evolution electrocatalyst, J. Am. Chem. Soc. 137 (2015) 7448–7455, http://dx.doi.org/10.1021/jacs.5b03545.
[24] L. Pavić, A. Moguš-Milanković, P. Raghava Rao, A. Šantić, V. Ravi Kumar, N. Veeraiah, Effect of alkali-earth modifier ion on electrical, dielectric and spectroscopic properties of Fe_2O_3 doped Na_2SO_4–MO–P_2O_5 glass system, J. Alloy. Compd. 604 (2014) 352–362, http://dx.doi.org/10.1016/j.jallcom.2014.03.061.
[25] P. Stoch, W. Szczerba, W. Bodnar, M. Ciecinska, A. Stoch, E. Burkel, Structural properties of iron–phosphate glasses: spectroscopic studies and ab initio simulations, Chem. Phys. 16 (2014) 19917–19927, https://pubs.rsc.org/en/content/articlehtml/2014/cp/c4cp03113j.
[26] D.M. Pickup, R.J. Newport, E.R. Barney, K. Ji-Yung, S.P. Valappil, J.C. Knowles, Characterisation of phosphate coacervates for potential biomedical applications, J. Biomater. Appl. 28 (2014) 1226–1234, https://journals.sagepub.com/doi/full/10.1177/0885328213502586.
[27] S.H. Santagneli, J. Ren, M.T. Rinke, S.J.L. Ribeiro, Y. Messaddeq, H. Eckert, Structural studies of $AgPO_3$–MoO_3 glasses using solid state NMR and vibrational spectroscopies, J. Non-Cryst. Solids 358 (2012) 985–992, http://dx.doi.org/10.1016/j.jnoncrysol.2012.01.031.
[28] B. Eraiah, Optical properties of lead-tellurite glasses doped with samarium trioxide, Bull. Mater. Sci. 33 (2010) 391–394, https://link.springer.com/article/10.1007/s12034-010-0059-z.
[29] M. Abdel-Baki, F.A. Abdel-Wahab, A. Radi, F. El-Diasty, Factors affecting optical dispersion in borate glass systems, J. Phys. Chem. Solids 68 (2007) 1457–1470, http://dx.doi.org/10.1016/j.jpcs.2007.03.026.
[30] S. Marzouk, S.M. Abo-Naf, M. Hammam, Y.A. El-Gendy, N.S. Hassan, FTIR spectra and optical properties of molybdenum phosphate glasses, J. Appl. Sci. Res. 7 (2011) 935–946, http://www.aensiweb.com/old/jasr/jasr/2011/935-946.pdf.
[31] M. Hafid, T. Jermouni, N. Toreis, T. Ghailassi, Structure of $(45-x)7Na_2O$–xBaO–5ZnO–$50P_2O_5$ glasses studied by DSC and infrared spectroscopy, Matter. Lett. 56 (2002) 486, http://dx.doi.org/10.1016/S0167-577X(02)00537-2.
[32] N. Ait Hana, M. Taibi, J. Aride, Thermal and spectroscopic characterization of glass system PbO–CaO–B_2O_3–P_2O_5, J. Mater. Environ. Sci. 5 (2014) 2000–2007, http://www.jmaterenvironsci.com/Document/vol5/vol5_N6/248-JMES-1310-2014-AitHana.pdf.
[33] L. She-Bao, W. Peng-Fei, S. Jiang-Bo, G. Hai-Tao, X. Shen-Nuo, Z. Peng-Fei, Y. Cheng-Long, L. Chun-Xiao, B. Peng, Spectroscopic and thermal properties of Yb^{3+} doped TeO_2–Bi_2O_3–Nb_2O_5 based tellurite glasses, J. Lumin. 153 (2014) 29–33, http://dx.doi.org/10.1016/j.jlumin.2014.02.031.
[34] A. Mishra, J. Rocherullé, J. Massera, Ag-doped phosphate bioactive glasses: thermal, structural and in-vitro dissolution properties, Biomed. Glasses 2 (2016) 38–48, https://www.degruyter.com/downloadpdf/j/bglass.2016.2.issue-1/bglass-2016-0005/bglass-2016-0005.pdf.
[35] A. Mogus-Milankovic, A. Santic, A. Gajovic, D.E. Day, Spectroscopic investigation of MoO_3–Fe_2O_3–P_2O_5 and SrO–Fe_2O_3–P_2O_5 glasses, J. Non-Cryst. Solids 325 (2003) 76–84, http://dx.doi.org/10.1016/S0022-3093(03)00362-4.

[36] E.L. Simmons, Diffuse reflectance spectroscopy: a comparison of the theories, App. Optics 14 (1975) 1380–1386, http://dx.doi.org/10.1364/AO.14.001380.
[37] S. Saha, A.K. Bhunia, Synthesis of Fe_2O_3 nanoparticles and study of its structural, optical properties, J. Phys. Sci. 17 (2013) 191–195, http://inet.vidyasagar.ac.in:8080/jspui/handle/123456789/881.
[38] N.A.M. Barakat, M.S. Khil, F.A. Sheikh, K. Hak Yong, Synthesis and optical properties of two cobalt oxides (CoO and Co_3O_4) nanofibers produced by electrospinning process, J. Phys. Chem. C112 (2008) 12225–12233, https://pubs.acs.org/doi/abs/10.1021/jp8027353.
[39] A.M. Abdelghany, H.A. ElBatal, R.M. Ramadan, The effect of Li_2O and LiF on structural properties of cobalt doped borate glasses, J. King Saud. Univ. Sci. 29 (2017) 510–516, http://dx.doi.org/10.1016/j.jksus.2016.09.003.
[40] G. Rama Sundari, D.V. Sathish, T. Raghavendra Rao, Ch. Rama Krishna, Ch. Venkata Reddy, R.V.S.S.N. Ravikumar, Characterisation of Fe^{3+} doped mixedalkali zinc borate glasses-physical and spectroscopicinvestigations, J. Non-Cryst. Solids 365 (2013) 6–12, http://dx.doi.org/10.1016/j.jnoncrysol.2013.01.023.
[41] K. Sambasiva Rao, N. Krishna Mohan, N. Veeraiah, Physical properties of $(Li_2O)_{0.40}(Fe_2O_3)_{0.05-x}(P_2O_5)_{0.55}(Ag_2O)_x$ glasses, Turk. J. Phys. 31 (2007) 11–29, http://journals.tubitak.gov.tr/.
[42] T. Dippong, E. Levei, O. Cadar, Thermal behavior of Ni, Co and Fe succinates embedded in silica matrix, J. Therm. Anal. Calorim. 136 (2019) 1587–1596, http://dx.doi.org/10.1007/s10973-019-08117-8.
[43] K. Eunah, Z.T.K. Jiang, NO measurement and calculation of optical band gap of chromium aluminum oxide films, Jpn. J. Appl. Phys. 39 (2000) 4820–4825, http://dx.doi.org/10.1143/JJAP.39.4820.
[44] F. Urbach, The long-wavelength edge of photographic sensitivity and of the electronic absorption of solids, Phys. Rev. 92 (1953) 1324, http://dx.doi.org/10.1103/PhysRev.92.1324.
[45] B. Bhatia, S.L. Meena, V. Parihar, M. Poonia, Optical basicity and polarizability of Nd^{3+}-doped bismuth borate glasses, New J. Glass Ceram. 5 (2015) 44–52, http://dx.doi.org/10.4236/njgc.2015.53006.
[46] H.A. Abd El-Ghany, Physical and optical characterization of manganese ions in sodium–zinc–phosphate glass matrix, Int. Adv. Res. J. Sci. Eng. Technol. 5 (12) (2018), http://dx.doi.org/10.17148/IARJSET.2018.5127.
[47] I.O. Gúth, S.R. Lukič, The influence of iron on the optical energy gap in glasses of Sb–S–I type, J. Optoelectron. Adv. Mater. 3 (2001) 903–908.
[48] Y.H. Elbashar, H.A. Abd El-Ghany, Optical spectroscopic analysis of Fe_2O_3 doped CuO containing phosphate glass, Opt. Quant. Electron. 49 (2017) 310, http://dx.doi.org/10.1007/s11082-017-1126-0.
[49] J.F. Stebbins, P. Zhao, S. Kroeker, Non-bridging oxygens in borate glasses: characterization by 11B and 17O MAS and 3QMAS NMR, Solid State Nucl. Mag. 16 (2000) 9–19, http://dx.doi.org/10.1016/S0926-2040(00)00050-3.
[50] M.A. Marzouk, S. Ibrahim, Y.M. Hamdy, Luminescence efficiency growth in wide band gap semiconducting Bi_2O_3 doped Cd0.4Pb0.1B0.5 glasses and effect of γ-irradiation, J. Mol. Struct. 1076 (2014) 576–582, http://dx.doi.org/10.1016/j.molstruc.2014.08.022.
[51] E.A. Davis, N.F. Mott, Conduction in non-crystalline systems. V. Conductivity, optical absorption and photoconductivity in amorphous semiconductors, Philos. Mag. 24 (1970) 903, http://dx.doi.org/10.1080/14786437008221061.
[52] P.B. Nair, V.B. Justinvictor, G.P. Daniel, K. Joy, V. Ramakrishnan, D.D. Kumar, P.V. Thomas, Structural, optical, photoluminescence and photocatalytic investigations on Fe doped TiO_2 thin films, Thin Solid Films 550 (2014) 121–127, http://dx.doi.org/10.1016/j.tsf.2013.10.112.
[53] G. Phaomei, W. Rameshwor Singh, N. Shanta Singh, R.S. Ningthoujam, Luminescence properties of Ce^{3+} co-activated $LaPO_4$:Dy^{3+} nanorods prepared indifferent solvents and tunable blue to white light emission from Eu^{3+} co-activated $LaPO_4$:Dy^{3+}, Ce^{3+}, J. Lumin. 134 (2013) 649–656, http://dx.doi.org/10.1016/j.jlumin.2012.07.014.
[54] S. Thielemans, D. Di Zenobio, A. Touhafi, P. Lataire, K. Steenhaut, DC grids for smart led-based lighting: the Edison solution, Energies 10 (2017) 1454, http://dx.doi.org/10.3390/en10101454.
[55] S. Nakamura, M. Senoh, S. Nagahama, T. Matsushita, H. Kiyouku, Y. Sugimoto, T. Kozaki, H. Umemto, M. Sano, T. Mukai, Violet InGaN/GaN/AlGaN-based laser diodes operable at 50 °C with a fundamental transverse mode, Jpn. Appl. Phys. 38 (1999) L226–L229, http://dx.doi.org/10.1143/JJAP.38.L226.
[56] R. Nomoto, Effect of light wavelength on polymerization of light-cured resins, Dent. Mater. J. 111 (1997) 60–73, http://dx.doi.org/10.4012/dmj.16.60.
[57] T.H. Margrain, M. Boulton, J. Marshall, D.H. Sliney, Do blue lightfilters confer protection against age-related macular degeneration, Prog. Retin. Eye Res. 23 (2004) 523–531, http://dx.doi.org/10.1016/j.preteyeres.2004.05.001.
[58] A. Moguš-Milanković, L. Pavić, K. Srilatha, C. Srinivasa Rao, T. Srikumar, Y. Gandhi, N. Veeraiah, Electrical, dielectric and spectroscopic studies on MnO doped LiI–AgI–B_2O_3 glasses, J. Appl. Phys. 111 (2012), 013714, https://doi.org/10.1063/1.3676254.
[59] J.B. Jorcin, M.E. Orazemb, N. Pébère, B. Tribollet, CPE analysis by local electrochemical impedance spectroscopy, Electrochim. Acta 51 (2006) 1473–1479, http://dx.doi.org/10.1016/j.electacta.2005.02.128.
[60] N.B. Pimentel, V.R.V.R. Mastelaro, J.C.J. M'Peko, S.W. Martin, S.S. Rojas, J.E. De Souza, Structural and electrical characterization of glasses in the Li_2O–CaO–B_2O_3 system, J. Non-Cryst. Solids 499 (2018) 272–277, http://dx.doi.org/10.1016/j.jnoncrysol.2018.07.024.
[61] N.N. Aye, Study of $xP_2O_5(1-x-y)V_2O_5yCuO$ semi-conducting glass system, Univ. Res. J. 4 (2011) 4.
[62] P. Bergo, S.T. Reis, W.M. Pontuschka, J.M. Prison, C.C. Motta, Dielectric properties and structural features of barium-iron phosphate glasses, J. Non-Cryst. Solids 336 (2004) 159–164, http://dx.doi.org/10.1016/j.jnoncrysol.2004.02.008.
[63] L. Pavic, A. Moguš-Milankovic, P. Raghava Rao, A. Šantic, V. Ravi Kumar, N. Veeraiah, Effect of alkali-earth modifier ion on electrical, dielectric and spectroscopic properties of Fe_2O_3 doped Na_2SO_4–MO–P_2O_5 glass system, J. Alloy. Compd. 604 (2014) 352–362, http://dx.doi.org/10.1016/j.jallcom.2014.03.061.
[64] T. Badapanda, R. Harichandan, T.B. Kumar, S.R. Mishra, S. Anwar, Dielecric relaxation and conduction mechanism of dysprosium doped barium bismuth titanate Aurivillius ceramics, J. Mater. Sci: Mater. Electron. 28 (2017) 2775–2787, http://dx.doi.org/10.1007/s 10854-016-5858-6.
[65] R.V. Barde, K.R. Nemade, S.A. Waghuley, AC conductivity and dielectric relaxation in V_2O_5–P_2O_5–B_2O_3 glasses, J. Asian Ceram. Soc. 3 (2015) 116–122, http://dx.doi.org/10.1016/j.jascer.2014.11.006.
[66] K. Srinivas, P. Sarah, S.V. Suryanarayana, Impedance spectroscopy study of polycrystalline $Bi_6Fe_2Ti_3O_{18}$, Bull. Mater. Sci. 26 (247) (2003), https://link.springer.com/article/10.1007/BF02707799.
[67] A. Radon', D. Łukowiec, M. Kremzer, J. Mikuła, P. Włodarczyk, Electrical conduction mechanism and dielectric properties of spherical shaped Fe_3O_4 nanoparticles synthesized by

co-precipitation method, Materials 11 (2018) 735, http://dx.doi.org/10.3390/ma11050735.
[68] Y. Ben Taher, A. Oueslati, N.K. Maaloul, K. Khirouni, M. Gargouri, Conductivity study and correlated barrier hopping (CBH) conduction mechanism in diphosphate compound, Appl. Phys. A 120 (2015) 1537–1543, http://dx.doi.org/10.1007/s00339-015-9353-3.
[69] M.I. Mohammed, Kh. Abd-Allah, M.Y. Hassaan, The conduction mechanism and dielectric behavior of sodium borate glasses containing Fe and Bi ions, Egypt. J. Solids 27 (2004) 2, http://egmrs.powweb.com/EJS/PDF/vo272/299.pdf.
[70] B.O. Sh Aziz, Gh. Abdullah, S.R. Saeed, H.M. Ahmed, Electrical and dielectric properties of copper ion conducting solid polymer electrolytes based on chitosan: CBH model for ion transport mechanism, Int. J. Electrochem. Sci. 13 (2018) 3812–3826, doi:10.20964/2018.04.10.
[71] O. Hafef, Z. Jaafar Othman, M. Megdich, A. Matoussi, Conduction mechanism and dielectric properties of ZnO/MgO solid composites, Appl. Phys. A 123 (2017) 95, http://dx.doi.org/10.1007/s00339-016-0721-4.
[72] K.P. Padmasree, D.K. Kanchan, Modulus studies of CdI_2–Ag_2O–V_2O_5–B_2O_3 system, Mater. Sci. Eng. B 122 (2005) 24–28, http://dx.doi.org/10.1016/j.mseb.2005.04.011.
[73] J. Robertson, High dielectric constant oxides, Eur. Phys. J. Appl. Phys. 28 (2004) 265–291, https://web.stanford.edu/class/ee311/NOTES/Robertson%20JAP04.pdf.
[74] S. Jayanthi, T.R.N. Kutty, Giant dielectrics from modified boundary layers in *n*-$BaTiO_3$ ceramics involving selective melting reactions of silver/glass composites at the grain boundaries, J. Mater. Sci.: Mater. Electr. 16 (2005) 269–279, http://dx.doi.org/10.1007/s10854-005-0544-0.
[75] A.K. Behera, N.K. Mohanty, B. Behera, P. Nayak, Structural and electrical properties of $KCa_2Nb_5O_{15}$ ceramics, Adv. Mater. Lett. 4 (2013) 141–145, https://link.springer.com/article/10.2478/s11534-008-0030-4.
[76] J.E. Kim, S.J. Kim, H.W. Choi, Y.S. Yang, Electrical conductivity spectra of $4BaTiO_3$–SiO_2 glass, J. Korean Phys. Soc. 42 (2003) S1224–S1227, https://inis.iaea.org/search/search.aspx?orig_q=RN:35064290.
[77] R. Bergman, General susceptibility functions for relaxations in disordered systems, J. Appl. Phys. 88 (2000) 1356–1365, http://dx.doi.org/10.1063/1.373824.
[78] L. Bih, L. Abbas, A. Nadiri, Y. El amraoui, D. Mezzane, H. Khemakhem, dc and ac conductivities of the yLi_2O–$(1-y)[0.35(MoO_3)_2$–$0.65(P_2O_5)$ glasses, M. J. Condens. Mater 7 (2006) 1, https://revues.imist.ma/?journal=MJCM&page=article&op=view&path%5B%5D=166&path%5B%5D=0.
[79] M.D. Ediger, C.A. Angell, R. Sidney, Nagel, Supercooled liquids and glasses, J. Phys. Chem. 100 (1996) 13200–13212, http://dx.doi.org/10.1021/jp953538d.